Experimental Investigation of Droplet Distributions from a Plunging Breaker with Different Wind Conditions

Reyna Guadalupe Ramirez de la Torre[1,1,1], Petter Vollestad[1,1,1], and Atle Jensen[1,1,1]

[1]University of Oslo

November 30, 2022

Abstract

Understanding the droplet cloud and spray dynamics is important on the study of the ocean surface and marine boundary layer. Several of the relevant phenomena depend highly on the characteristics of the spray produced by waves. Nonetheless, the role that the wave energy and the type of wave breaking plays in the resulting distribution and dynamics of droplets is yet to be understood. The aim of this work was to generate violent plunging breakers in the laboratory, quantify the produced droplets, obtaining their sizes and dynamics and to analyze the effect of the different wind speeds on the droplet production. It was found that the mean radius increases with the wave energy and the shape of the initial distribution of droplet sizes does not change with the presence of wind. Also, indications of turbulence affecting the droplet dynamics at wind speeds of 5m/s were found. The amount of large droplets (radius > 1mm) found in this work was larger than expected from the literature. An improved estimation of the initial distribution of large droplets can largely affect the evolution of the Sea Spray Generation Function, and therefore the estimation of energy and mass transport in the marine boundary layer.

Experimental Investigation of Droplet Distributions from a Plunging Breaker with Different Wind Conditions

R.G. Ramirez de la Torre [1], P. Vollestad[1], A. Jensen[1]

[1]University of Oslo

Key Points:

- Initial Droplet Size Distribution
- Focusing Wave Train
- Spray Generation

Corresponding author: R.G. Ramirez de la Torre, `reynar@math.uio.no`

Abstract

Understanding the droplet cloud and spray dynamics is important on the study of the ocean surface and marine boundary layer. The role that the wave energy and the type of wave breaking plays in the resulting distribution and dynamics of droplets is yet to be understood. The aim of this work was to generate violent plunging breakers in the laboratory and analyze the spray production by the crest of the wave when it impacts in the free surface. The droplet sizes and their dynamics were measured and the effect of different wind speeds on the droplet production was also considered. It was found that the mean radius increases with the wave energy and the presence of larger droplets (radius > 2 mm) in the vertical direction increases with the presence of wind. Furthermore, the normalized distribution of droplet sizes is consistent with the distribution of ligament-mediated spray formation. Also, indications of turbulence affecting the droplet dynamics at wind speeds of $5\,\mathrm{ms^{-1}}$ were found. The amount of large droplets (radius > 1 mm) found in this work was larger than reported in the literature. An improved estimation of the initial distribution of large droplets can largely affect the evolution of the Sea Spray Generation Function, and therefore the estimation of energy and mass transport in the marine boundary layer.

Plain Language Summary

When ocean waves break, a large amount of bubbles and droplets is produced. The created droplets can travel very far distance and very long times depending on their sizes and the wind conditions. These droplets are an important factor for the changes in the weather close to the water surface but also to changes in the global atmosphere. Temperature, humidity, salinity are only some of the examples of the weather conditions that depend on the droplet presence and movement through the atmosphere. In our study, we try to estimate how many droplets detach from the waves when they break and which sizes do they have. We also try to understand the role of wind in these initial instants. We found that the sizes of the produced droplets are larger than presented in previous research. We also found that the presence of wind is not as important as the wave energy in the production of the different sizes. The characteristics of the droplets produced from wave breaking are very important to understand their evolution through time and their transportation through the atmosphere. Further study of these characteristics will help to produce more accurate models to predict changes in the atmosphere.

1 Introduction

At the ocean surface, a large range of complex two phase flow interactions generate aeration in the ocean and aerosol transport through the air. In the present study, we are interested in wave breaking and marine icing processes. For example, in the Arctic environment the droplets produced after wave breaking are transported by the wind and generate thick layers of ice over the surface of ships and structures in short time. These ice-layers represent a life hazard for the inhabitants of these vessels. Field studies and simulations has been used to address this phenomenon (Rashid et al., 2016; Dehghani et al., 2016; Bodaghkhani et al., 2016; Ryerson, 1990), but its complexity has shown that a deeper understanding of the droplet generation is necessary. The study of droplet size distribution and dynamics becomes important to understand the transport through the marine boundary layer and above. To make models of this phenomena, there is need of more information about the size and velocity distributions of the particles. These type of measurements or estimations can be useful when developing numerical models for marine icing, for example. Small droplets can be transported over long distances and remain in the atmosphere for several days, while large droplets remain close to the ocean surface and return to the ocean in shorter time scales but still affect the air-sea fluxes of momentum and enthalpy (Veron, 2015).

Some of the relevant articles for this study were Fairall et al. (2009), Stokes et al. (2013) and Veron et al. (2012) which presented experimental results on spray size distributions and Sea Spray Generation Function (SSGF) produced by different setups: wind generated waves, mechanical generated waves with wind, plunging planar jet, etc. More recently Ortiz-Suslow et al. (2016) conducted an experimental study with mechanical waves and winds up to $54\,\mathrm{ms}^{-1}$. The findings of Ortiz-Suslow et al. (2016) showed a similar power law as the proposed before with an important dependence on the wind velocity. Nonetheless, for droplets with radii $\sim 1\,\mathrm{mm}$, the production rates were several orders of magnitude higher than the rates expected from previous investigations (Fairall et al., 2009; Veron, 2015). The droplets were measured at locations between 2 and 6 times the local significant amplitude, and for the highest wind speeds droplets with radius $\sim 1\,\mathrm{mm}$ were observed in relatively high quantities at 3–4 times the significant wave height. Furthermore, field measurements have been conducted, where the concentration of aerosol numbers in the atmospheric boundary layer were obtained (Lenain & Melville, 2017). Droplets sizes ranging from 0.1 to 200 microns were considered. It was found that droplets with radii larger than 40 microns can reach heights higher than 400 m above mean sea level. These findings may suggest that large droplets have a longer lifetime in the atmospheric boundary layer than previously expected. Therefore, the processes from where these larger droplets are created need to be better understood.

In the review, Veron (2015), previous findings and emerging consensus on sea spray generation were summarized. Three types of sea spray production processes are thoroughly analyzed: Film, Jet and Spume produced droplets with radius up to 1mm. These small droplets (radius $< 1\,\mathrm{mm}$) have residence times in the atmospheres from minutes to several days, or even weeks –when the radius is only a few nanometers. The long residence times allow to make direct estimations of the spray size dependence on the wind velocities by measuring the drop concentration average profile through time. The review also summarizes thoroughly the studies over direct and indirect methods to estimate a SSGF. It is pointed out, that indirect estimations of the SSGF have the common assumption of a universal source function, and that the change on number density for a particular size range is considered to depend only on other controlling parameters, such as wind speed, fetch, surface stress, etc. The review closes by highlighting that one of the main issues to study in the future is the large spume droplets (radius larger than $1\,\mathrm{mm}$), their generation mechanism, initial velocity and dynamic behaviour through the airflow. Moreover, field studies of droplet distribution on vessels showed that the sizes distributions extend to several millimeters (Bodaghkhani et al., 2016; Ryerson, 1990). The study of larger droplets generation, their trajectories and velocities is relevant for the understanding of phenomena that occurs close to the ocean surface. For example, the main source of marine icing on ships and offshore structures is the sea spray generated by breaking waves and waves impacting in the same structures (Bodaghkhani et al., 2016; Rashid et al., 2016). The present study is an attempt to contribute to the understanding of the large droplets behaviour. In particular the generation mechanism, initial size distribution, or so called source function, and the dynamic behaviour through the airflow.

There are several studies of droplet size distribution and SSGF available, probably the most relevant for this study were Mueller and Veron (2009) and Villermaux et al. (2004) where the importance on the initial distribution or source function to estimate the shape of the SSGF was addressed. Villermaux et al. (2004) proposed a Γ-distribution to fit the droplets created after the break-up and coalescence of what they called *ligaments* that detached from the main water bulk. They show the dependence of the droplet distribution on the volume and diameter of these ligaments independently of the shape of the liquid bulk. Then, Mueller and Veron (2009) used the proposed Γ-distribution as the initial distribution to calculate the shape of the SSFG. They found their proposed function implied considerably larger energy fluxes at low and moderate winds. These findings remark the importance of the individual processes of production and suspension of droplets and point towards the complexity of the initial size distributions due to the variety of such processes.

The importance of the dynamics of the droplet generation and transport has also been studied. The description of dispersion and transport of droplets has been done by examining the motion of a single drop and quantifying the influence of the airflow and turbulence over the droplet. Equations for terminal velocities and drag coefficients have been obtained and related to Particle Reynolds numbers (Re), Stokes numbers (St) and the Kolmogorov time scaling (Clift et al., 2005; Andreas et al., 2010; Crowe et al., 2011). But when dealing with large numbers of droplets, it is also important to consider the statistics of the phenomena. In general, particles moving in a fully developed turbulent flow have velocity components that are Gaussian distributed and the speed follows the Maxwell-Boltzman distribution, similarly to the Brownian motion (Pope, 1994). Also, it has been found that the acceleration components has a stretched exponential shape with largely extended tails compared to a Gaussian distribution (La Porta et al., 2001). This is a phenomenological function for flows with $200 \leq R_\lambda \leq 970$, where R_λ is the Taylor microscale Reynolds number defined in terms of Reynolds number of the flow Re_{flow} as $R_\lambda = (15Re_{flow})^{1/2}$. This function has been experimentally confirmed by different articles through out different fluid dynamics applications (Voth et al., 2001; Mordant et al., 2004; Shnapp et al., 2019; Kim & Chamorro, 2019).

In this study we present experimental results for medium and large droplets ($0.25\,\mathrm{mm} \leq r \leq 5.5\,\mathrm{mm}$) generated by plunging breakers. When the crest of the plunging breakers impact the free surface, a large quantity of spray is produced. Cases without wind and with the presence of low wind ($<7\,\mathrm{ms^{-1}}$) have been studied. We attempt to find the shape of the initial size distribution, or source function, and relate the conditions at the source (like wave energy content and wind) to the dynamics of the droplets. Our work is structured as follows. In section 2, the experimental setup is presented thoroughly. First, the generation of wind and its resultant profiles are detailed. Then, the generation of the focusing wave train and its development in the presence of a beach and wind are presented. In section 3, we present the resultant dynamics and sizes obtained by the use of Three Dimensional Particle Tracking Velocimetry (3DPTV), these results are further analyzed to obtain statistical distributions of initial droplet diameter, vertical reach, velocity and accelerations.

2 Experimental Methods

The experiments were conducted in the Hydrodynamics Laboratory at the University of Oslo, in the wave tank with dimensions $25 \times 0.52 \times 1\,\mathrm{m}$ where the mean water level for all experiments was $0.5\,\mathrm{m}$. In this work violent plunging breakers are made and the produced droplets are quantified, obtaining their sizes and dynamics and analyzing the effect of the different wind speeds on the droplet production. To produce breaking waves, a focusing wave train is used, where long waves overtake short waves, further details can be found in Section 2.2. Then the breaking was made more violent by adding a slope which caused the already focused waves to steepen and overturn. The overturning crest of the wave splashed at the free surface releasing a large number of droplets. The experiment consisted of three main measuring techniques: the generation and analysis of a focusing wave train that steepens by the effects of a slope, the wind velocity profiles produced on top of the waves and the detection of the droplet cloud created after the break. Hereafter, the different analysis tools are described in detail.

2.1 Wind Profiles

The wind profiles, without the influence of mechanically generated waves, were measured using particle image velocimetry (PIV). The center of the field of view (FOV) is 10.75 meters from the wave paddle in the location "PIV FOV", indicated in figure 1. Two

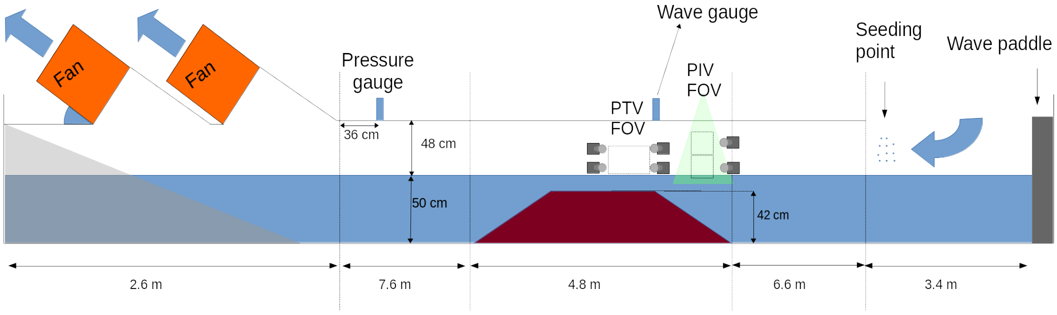

Figure 1. Schematic drawing of the wave tank in the Hydrodynamics Laboratory where the experiments were developed

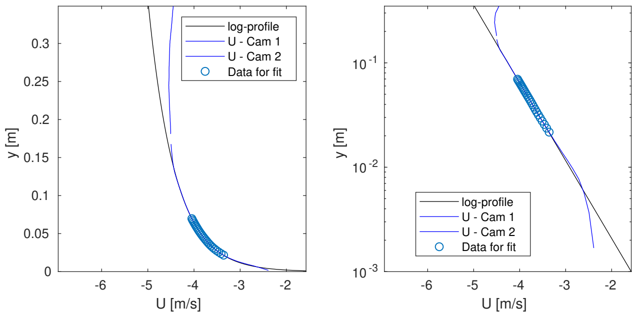

Figure 2. Example recorded velocity profile (blue lines), data points used for fit with equation 1 (blue circles) and resulting log-profile (black line). Illustrated with linear (left) and semilogarithmic (right) axis.

Photron WX100 (2048x2048 pixels) cameras with 50 mm lenses are used, each providing a FOV of approximately 18x18 cm. The cameras were positioned in a vertical arrangement, as indicated in figure 1. The air phase was seeded with small ($\approx 6\ \mu m$) water droplets generated from a high pressure atomizer. The centerplane was illuminated by a 147 mJ ND:YAG double pulsed laser. The cameras were set to acquire images at a rate of 30 fps, and a frame straddling technique was employed to control the effective Δt between an image pairs used for PIV. Hence, 15 velocity fields were acquired per second. Δt was varied between 150 and 350 μs depending on the air velocity in the flume. The images (800 per experimental case) were processed in Digiflow by Dalziel Research partners (Dalziel, 2017), with a final subwindow size of 80x80 pixels, and 50 % overlap.

The lower part of the velocity profiles (some distance above the waves) were found to be well represented by a logarithmic velocity profile:

$$u = \frac{u_*}{\kappa} \ln(y/y_0), \tag{1}$$

where u_* is the wind friction velocity, κ is the Von Karman constant (set equal to 0.41) and y_0 is the roughness height. Equation 1 was fitted to a part of the velocity profile exhibiting a logarithmic profile, deducing u_* and y_0, as shown in figure 2. The logarithmic profile was then used to estimate an equivalent U_{10} (mean velocity evaluated 10 meters above the surface). Results are presented in table 1, together with the peak horizontal velocity recorded (U_{max}).

Table 1. Results from the wind profile analysis.

Wind case	U_{max} [m/s]	u_* [m/s]	y_0 [mm]	U_{10} [m/s]
1	3.41	0.151	0.0185	5.14
2	3.91	0.201	0.0403	6.09
3	5.09	0.286	0.0984	8.03
4	5.45	0.308	0.1015	8.64
5	6.16	0.341	0.0864	9.70

Table 2. Maximum wave amplitude for the envelope at the focal point x_f, for the different voltage inputs in the wave paddle and maximum steepness ak considering all wave trains have $k = 7.59$ rad/m

Wave case	a_{max} [m]	ak
1	0.062	0.47
2	0.075	0.57
3	0.087	0.66

2.2 Generation of Focusing Wave Trains

The mechanically generated waves were created by a horizontal displacement wave paddle, shown in Figure 1. Focusing wave packets were created, the focal region is produced by generating waves whose period increased with increasing time. To modify the wave energy, different wave amplitudes were generated by varying the maximum voltage input V_m, the maximum amplitude a_{max} is shown in table 2. A group of focusing waves is created using this input voltage time history (Brown & Jensen, 2001):

$$V(t) = b(t) \sin \Phi(t) \tag{2}$$

for $0 \leq t \leq t_s$ with

$$b(t) = \frac{256}{27} \frac{t^3(t_s - t)}{t_s^4} V_m \tag{3}$$

$$\Phi(t) = 2\pi f_0 t \left(1 - \alpha \frac{t}{t_s}\right) \tag{4}$$

where the instantaneous wave frequency is approximately

$$\omega(t) = \frac{d\Phi}{dt} = 2\pi f_0 \left(1 - 2\alpha \frac{t}{t_s}\right) \tag{5}$$

Under deep water conditions, $\omega(t)$ produces a perfect focus at

$$x_f = \frac{g t_s}{8\pi\alpha f_0} \tag{6}$$

therefore, to define x_f, the parameters α, t_s and f_0 should be constant. In these experiments, the parameters were defined as:

$$\alpha = 0.30, \quad t_s = 18\,\mathrm{s}, \quad f_0 = 2Hz,$$

which defined the focal point at $x_f = 11.69\,\mathrm{m}$, approximately the edge of the sloping beach. It is important to notice that the wave number k is only dependent of $\omega(t)$ in eq. 5; therefore, using the dispersion relation for intermediate depth: $\omega^2 = gk \tanh(kh)$, values of k can be calculated numerically for each instant in the wave packet. $k = 7.59$ rad/m at the breaking point for all cases.

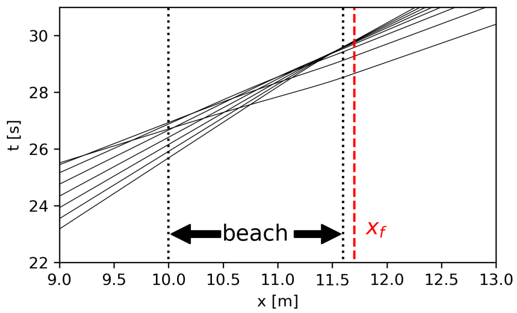

Figure 3. Phase space of focusing wave train, the beach position is limited by the dotted line and the position of the original focusing point x_f is shown with the red line.

By using this focusing method, we obtain breaking waves when we reach steepness $ak > 0.44$. But the breaking created by the selected amplitudes only generated spilling breakers and small overturning. It is worth mentioning, that larger amplitudes cannot be used, because the wave packets break before reaching the focal point. Therefore, a shoaling was added to steepen the waves even more as they approach the focusing point. In this way, the waves are forced to overturn as the toe of the wave decelerates and the crest accelerates. Nonetheless, it was expected that the presence of the beach affected the focus position as we approach to shallow waters, so the effect of the shoaling at the breaking point should be studied. The phase space in figure 3, shows the effects of the sloping beach at the focal point. This diagram shows that some of the frequencies will reach x_f faster due to the presence of the beach. Nonetheless, most of the frequencies preserve the original x_f.

Additionally, the surface elevation at x_f for the wave groups with and without beach can be compared (figure 4, to the left). It is visible that the caustic or envelope suffers some modifications. In this figure $ak = 0.57$ has been selected as example. The solid line shows the packet previous to the presence of the beach ("no-beach" label in figure) and the dashed line shows the wave packet when the beach is added. The steepening effect is visible in the second case. But the central high component remains and produces a violent plunger breaker that can be studied. The energy content of the wave group can be quantified by means of the power spectrum. Figure 4(right) shows the power spectrum of the wave groups at x_f for the example case ($ak = 0.57$). It is obvious that both cases have the same peak frequency, but the beach case shows evidence of energy dispersion, which was expected. Over all, the presence of the beach affects the energy and spectrum of the group but not the position of the breaking point.

2.3 Wind Generated Waves and their Influence in the Focusing Wave Train

When introducing wind in the air phase, it was expected to obtain a field of wind generated waves. Their characteristics will depend on the wind velocity U_{max} and the fetch, as has been studied in wave theory. The wind wave field will disturb the focusing packet and modify the frequencies and the energy present at the impact. Therefore it was important to quantify the influence of this field in the impact zone. Using the wave gauges, one minute time series of the surface elevation were taken for different wind speeds U_{max} without the presence of the focused packet. The power spectrum of these series is presented in figure 5. The spectra show that the peak frequency of the wave filed changes with the wind speed. For larger wind speed, the peak frequency decreases and the energy content increases. These frequencies are higher than those for the mechanical gen-

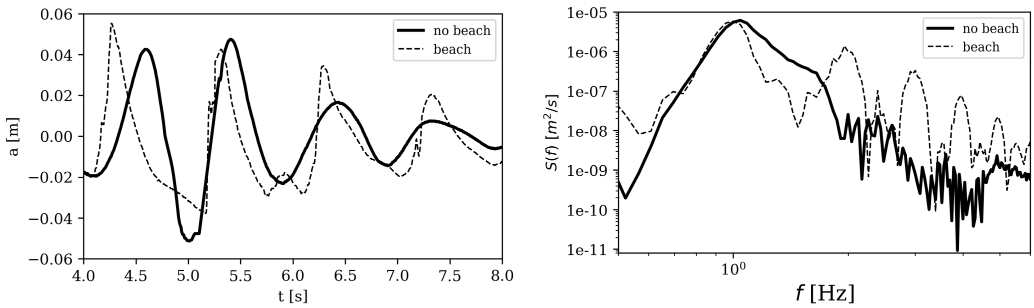

Figure 4. Surface elevation and Power Spectrum at the focal point. Comparison of the same wave amplitude before the beach is situated and after the beach is situated. With the beach presence the wave steepens and overturns to generate a plunger.

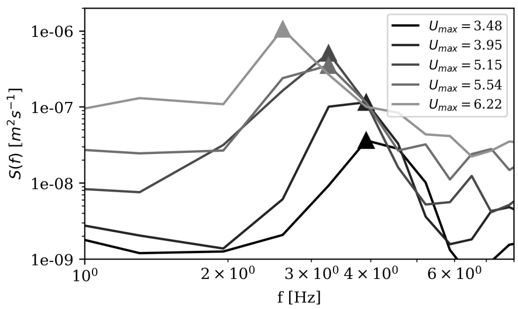

Figure 5. Power spectrum of the wind waves field without the presence of mechanically generated waves.

erated waves and the magnitude of the coefficients is at most of the same order. From these results, it could be interpreted that the wind could modify the energy content of the wave packet but the influence over the shape and focusing point of the mechanical waves could be minor. To confirm or refute this premise we can use again the surface elevation and the power spectrum to investigate the wave packet while wind is produced.

Figure 6 shows an example of the surface elevation and the power spectrum for the example steepness ($ak = 0.57$, same as figure 4). The graph shows the cases with wind velocity $U_{max} = 6.2\,\mathrm{ms}^{-1}$ (and beach) compared to the no-wind case (with beach) and the no-beach case. Both graphs show similar results to figure 4, the envelope shape has small changes and we can see a slight phase change for the highest components when wind is applied. The steepening of the wave from the no-wind case to the wind case is minor compared to the steepening from the beach case to the no-beach case. The frequency domain is also similar in all cases, they have the same peak frequency and the wind cases have dispersion that is indistinguishable from the dispersion created only by effects of the beach. In conclusion, the beach and wind presence affects the energy content of the wave group and therefore the energy of the breaker. To quantify the change in energy content of the different cases, we can use the mean power as defined by statistics:

$$R(0) = \int_{-\infty}^{\infty} S(f)df, \tag{7}$$

$R(0)$ is the area under the spectral curve, which can be interpreted as the energy content of the wave as $R(0) \propto a^2$ which is also proportional to the energy. Figure 7 shows the calculated $R(0)$ compared to the different maximum wave steepness: ak and wind

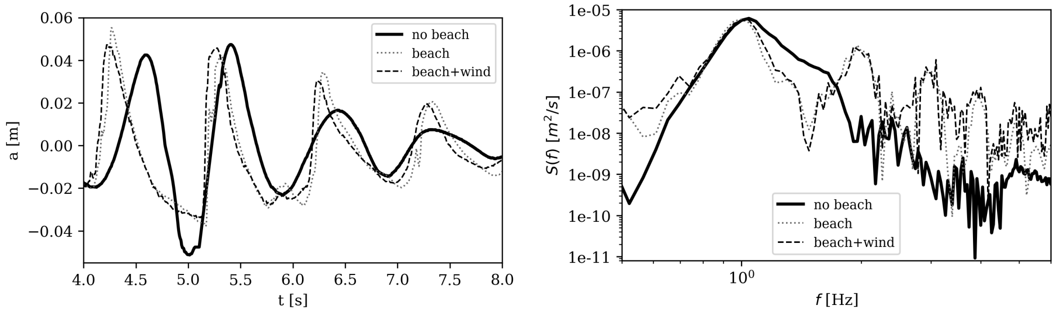

Figure 6. Surface elevation and Power Spectrum at the focal point for cases with wind. Comparison of the same wave amplitude before the beach is situated and after the beach is situated with addition of wind. With the beach, the wave steepens and overturns to generate a plunger. The presence of wind also affects the steepening but less significantly.

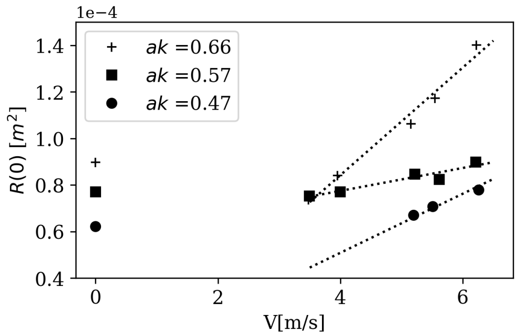

Figure 7. Mean power of the wave series against wind velocity. The different markers represents different wave amplitudes.

velocities: U_{max} used for this work. The graph shows the effect of wind over the wave energy. In all cases the energy increases with ak. But, it is interesting to see that for $U_{max} <$ 4.5 the total energy of the packet is less than the energy of the packet without the presence of wind. Table 3 shows the breaking type for all the cases analyzed. The difference between a small plunger and a plunger is the plunge distance. The plunge distance is defined as the distance from the break point to the crest touchdown point. We call the breaking type "small plunger" if the plunge distance is smaller than $a_{max}/2$. For the case of $ak = 0.47$ with wind velocities $U_{max} < 4.5\,\mathrm{ms}^{-1}$ do not generate a plunging breaker, therefore this data is not accounted in the study. The estimated energy will be compared to the results of the droplet clouds.

2.4 3DPTV

When the wave breaks, the crest accelerates and curls over the front. Then the crest impacts the free surface and it splashes creating a cloud of droplets. After the wave breaks, the disintegrating wave keeps moving forward and ejecting droplets from its surface. We analyze all the droplets that were visible in the selected FOV(fig. 1 and fig. 8), mainly the droplets generated by the splashing crest. The trajectories, velocities and accelerations of the droplets are obtained using 3DPTV. PTV uses the Langrangian approach to follow the droplets. 3-D coordinates can be obtained by using stereoscopic imaging and synchronous recording of the motion. The 3-D particle positions are tracked in the

Table 3. Type of breaking before and after adding the sloping beach and under different wind conditions.

Conditions	$ak = 0.47$	$ak = 0.57$	$ak = 0.66$
no beach	spilling	spilling	spilling
beach, $U_{max} = 0$	spilling	small plunger	small plunger
beach, $U_{max} = 3.41$	spilling	small plunger	plunger
beach, $U_{max} = 3.91$	spilling	plunger	plunger
beach, $U_{max} = 5.14$	small plunger	plunger	plunger
beach, $U_{max} = 5.45$	plunger	plunger	plunger
beach, $U_{max} = 6.22$	plunger	plunger	plunger

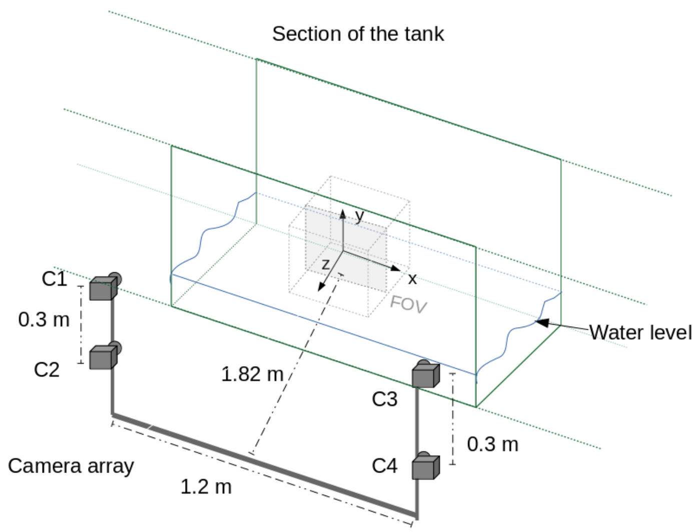

Figure 8. Schematic drawing of the 4-camera setup for 3DPTV.

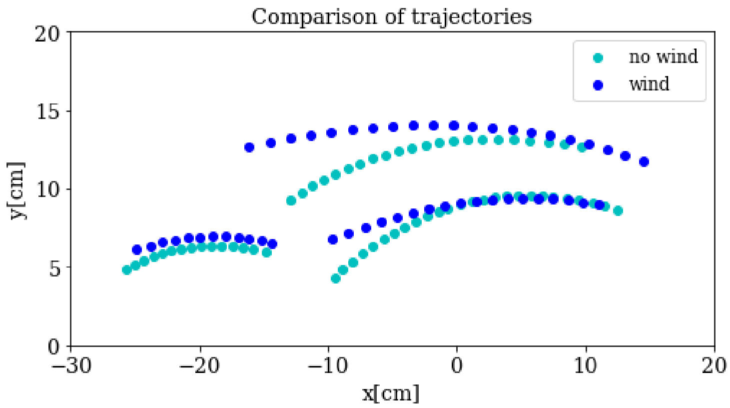

Figure 9. Qualitative comparison of the trajectories obtained for experiments with wind and experiment without wind

Table 4. Total number of droplets analyzed

	$U_{max} = 0\,\text{ms}^{-1}$	$U_{max} = 5.2\,\text{ms}^{-1}$	$U_{max} = 6.2\,\text{ms}^{-1}$
$ak = 0.47$	1518	10455	17310
$ak = 0.57$	8046	11001	10650
$ak = 0.66$	9154	13292	12272

time domain to derive the velocities and accelerations. A 4-camera system is used to perform 3DPTV, using the open source software OpenPTV (Consortium et al., 2012). Images of the cloud are taken by 4 Monochromatic AOS Promon cameras with 50mm lenses. The frame rate is 167 fps and the image resolution is 1920×1080pixels. The FOV right side is located on the breaking point to obtain all the splashing occurred in front of the wave, as shown in figure 1. The three-dimensional FOV is approximately $0.25 \times 0.15 \times 0.20$ m, as shown in Figure 8 where the FOV is represented by the gray outlined area. The gray plain represents the focal plain of the cameras which corresponds to the plain $z = 0$. It is important to mention that the direction of the waves and the wind is in the negative direction of the x-axis. A sequence of 2 seconds during and after the breaking is recorded. From the post processing we can also obtain size distributions of the droplet cloud. A set of 5 repetitions was developed for each wave amplitude and wind speed.

The breaking and spray generation process happens in a span of less than one second, and the physical event has an inherent randomness. Therefore the results of the 5 experiments are used as an ensemble in statistics. For each droplet we collect the results of the PTV processing (size, position, velocity and acceleration) in each time step. Every time step is also consider in the analysis. As it was expected, we observed the droplets are not always spherical and their deformation increases with the size. The equivalent diameter D_e is commonly used to classify droplet sizes with one unique parameter and is commonly defined as $D_e = \sqrt{ab}$, where a and b are the major and minor axis of the ellipsoid. In addition, to calculate the values of a and b we use an averaged value from the 4 images obtain by the camera array.

3 Results and Discussion

A sample of 3D trajectories are presented in Figure 9, the trajectories have parabolic shape when $U_{max} = 0$, but with the increasing wind speed the shape tends to be more

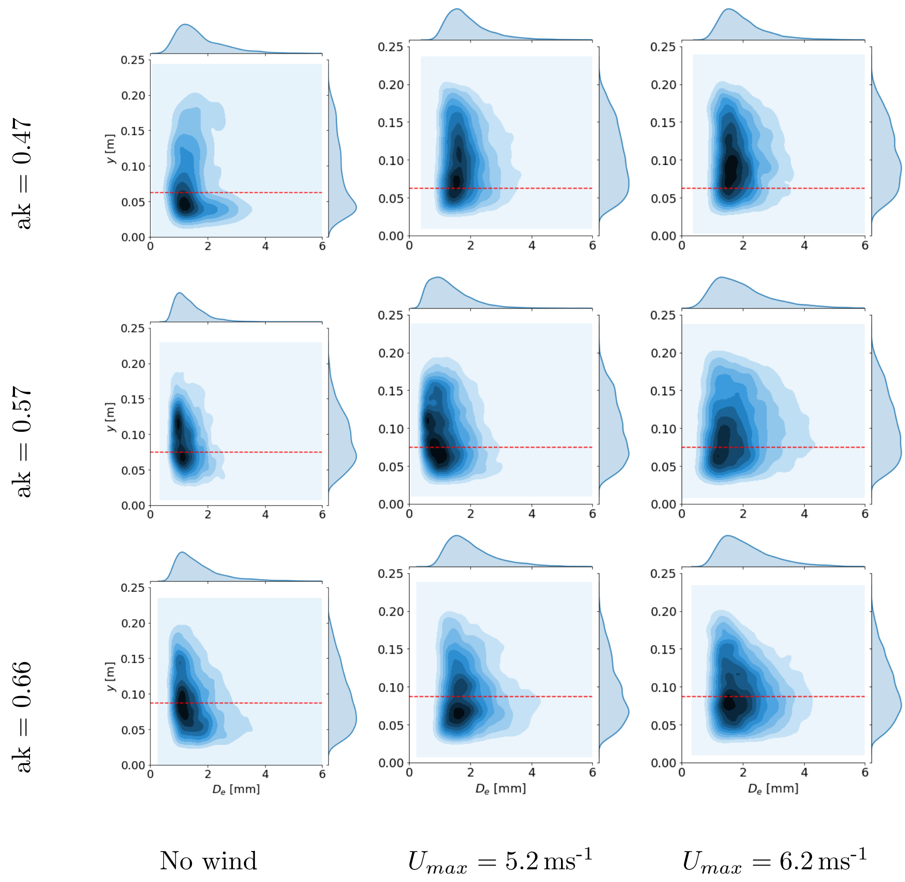

Figure 10. Equivalent Diameter D_e distribution versus height distribution for the different steepness ak and wind velocities U_{max}. The red dotted line represents the maximum wave height before breaking.

skewed. The total number of analyzed particles can be found in Table 4. From the table, the number of droplets produced in the impact appears to grow with presence of wind, but there is no apparent relation between the wave steepness and the number of droplets. This might be a consequence of the different breaking presented on each case, as presented in table 3. For example, $ak = 0.47$ is only spilling when $U_{max} = 0$ and $ak = 0.57$ is considered to be only a small plunger for the same case. Figure 10 shows the equivalent diameter D_e and height distributions of droplets for different cases, the vertical panels shows different wind speeds U_{max} and the different horizontal panels show different wave steepness ak. The maximum wave amplitude a_{max} is depicted with a red line. In all cases, higher concentrations of larger particles are presented when the wind is applied. When $U_{max} = 0$ the particles with $D_e > 2mm$ are clearly found only under a_{max}. In contrast, larger concentrations of these particles are found over a_{max} for the wind cases. This result agrees with the hypothesis that more droplets will be transported further by the wind. When $ak = 0.57$ the presence of large droplets is small compared to the other cases, this might be a consequence of the different types of breaking mechanisms. In this case the small plunger seems to produce less droplets than the spilling breaker. By visual inspection, the amount of spray is different, but it is difficult to quantify the difference in the breaking process.

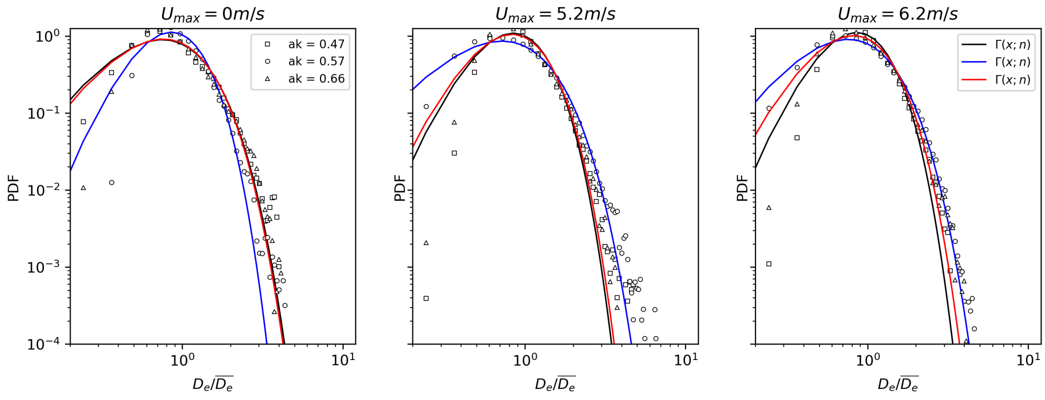

Figure 11. Probability Distribution of D_e compared to distribution proposed by Villermaux et al. (2004)and used in Mueller and Veron (2009)

Figure 11 shows the Probability Distribution for D_e, the solid lines correspond to the Γ-distributions as proposed by Villermaux et al. (2004):

$$\Gamma(x;n) = \frac{n^n x^{n-1} e^{-nx}}{\Gamma(n)} \tag{8}$$

where n^{-1} is the variance and $x = D_e/\overline{D_e}$ is the diameter normalized by the mean. Values of n lie between 3.5 and 7 and are similar to those in Villermaux et al. (2004). Another relation, proposed by in the mentioned study, was between n and the ratio $\overline{D_e}/\xi$, where ξ is the average diameter of a ligament. In a general, this relation can be expressed as:

$$N\frac{\overline{D_e}}{\xi} \simeq e^{\frac{n}{3}} \tag{9}$$

with N being a normalization factor that depends on the initial length of the ligament. Mueller and Veron (2009) presents the simplified relation: $n = 0.4(\overline{D_e}/\xi) + 2$. In our experiments ligaments are also created during the splash and after the wave breaking, ligaments with diameters between 1–5 mm have been found by manual inspection of the obtained images. Although the mechanism from which ligaments are generated may not be the same as for that presented in the mentioned study, the mechanism that forms droplets from the breakup of ligaments is suspected to be similar. Assuming that most of the droplets were generated by ligament breaking, and considering that the relation obtained by Mueller and Veron (2009) holds for this study, we can assume that the droplets with mean diameter $\overline{D_e}$ come from ligaments of diameter $\xi \approx 0.4$ mm. With a resolution of 0.15 mm per pixel in the images acquired, most of this ligaments would be barely detectable in the images.

Figure 12 shows $\overline{D_e}$ for the different cases. From the figure, it is observed that $\overline{D_e}$ increases with $R(0)$ of the wave, a simple first order polynomial fit can be made which results in the relation: $\overline{D_e} = 7.65R(0) + 0.001$ with a coefficient of determination of $R^2 = 0.36$. According to Mueller and Veron (2009): $D_0 \approx 2.5D_e$, where D_0 is the diameter of a sphere with the equivalent volume as the average ligament, assuming that this relation is sustainable in the present study, then $D_0 \approx 2.5\overline{D_e} = 2.5(7.65R(0) + 0.001)$ this means that the D_0 increases with $R(0)$, the energy of the wave packet. Previously, it has been found that the mean size of droplets decreases with the presence of high winds (Mueller & Veron, 2009; Ortiz-Suslow et al., 2016; Fairall et al., 2009). Our findings suggest that it is the break-up of larger droplets in the turbulent flows that contributes to the generation of smaller droplets. Therefore the study of large droplets breakup in high wind could be of interest.

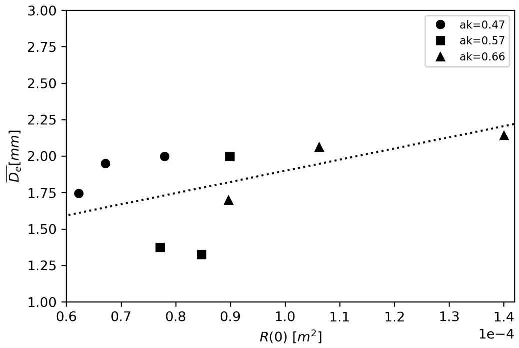

Figure 12. $R(0)$ against mean equivalent diameter. A linear fit is shown with the dotted line: $\overline{D_e} = 7.65R(0) + 0.001$ with $R^2 = 0.36$. The mean diameter seems to increase with the energy content of the wave packet.

3.1 Velocity Distributions

Figure 13 shows the probability distributions of the velocity components for all the droplets analyzed in the different cases. Each vertical panel shows the same U_{max} and each horizontal panel shows one of the velocity components. The different ak are shown with distinct markers and a solid line shows the Gaussian distribution with the same mean and standard deviation as the data. Only the cases with $U_{max} > 0$ exhibit similarity with the Gaussian distribution. Mean values for each velocity component has been calculated over the different sets corresponding to the same ak and U_{max}. The mean value is different for each velocity component, but consistent through the same U_{max} and independent of ak as shown in table 5. When $U_{max} = 0$ the probability for droplets with the mean velocity is larger than the estimated by the Gaussian distribution, especially in the u and w components which refer to the horizontal components. On the other hand, v the vertical component presents a larger probability for extreme cases when there is no wind. This means that the largest vertical velocity is dampened by the presence of wind. For all components, the standard deviation increases with U_{max}, which is more likely an indication of the forcing applied on the droplets by the wind, the forcing could be responsible of increasing the variability of the instantaneous velocities, creating larger deviations from the mean.

In this order, we could consider the flow regime in which the experiments were developed. The Reynolds number of the airflow can be estimated as $Re_{flow} = LU_{max}/\nu$, where L is the length of the section of the tank which contains air and ν is the kinematic viscosity of air. For the case were $U_{max} = 0$, Re_{flow} is zero, but instead we consider the maximum particle Reynolds number $Re = D_{max}|\vec{u}|_{max}/\nu$, where D_{max} is the maximum diameter of found droplets and $|\vec{u}|_{max}$ is the maximum speed for the droplets. These values are presented in Figure 13. From these values of Re_{flow}, both wind cases could be consider as turbulent flows. However, it might not be expected to see the effect of turbulent flow onto large droplets. Nonetheless, the results found for the velocity components resembles those found for tracer particles in turbulent flows (Voth et al., 2001; Ouellette et al., 2006).

From the velocity components, the speed $|\vec{u}|$ can be calculated and the distributions obtained are presented in Figure 14. The different ak are represented by different markers and the solid line represents the Maxwell-Boltzman(M-B) distribution with the same mean value. M-B distribution represents the speed of particles moving in three dimensions with Gaussian distributed velocity components. The top graphs show the distribution for $U_{max} = 0$ and the bottom graphs summarizes the results for the other cases.

Table 5. Mean of velocity components by U_{max} and velocity component

	$U_{max} = 0\,\mathrm{ms}^{-1}$	$U_{max} = 5.2\,\mathrm{ms}^{-1}$	$U_{max} = 6.2\,\mathrm{ms}^{-1}$
u	-0.39 m/s	-0.14 m/s	-0.29 m/s
v	-0.20 m/s	-0.17 m/s	-0.20 m/s
w	0.00 m/s	0.00 m/s	0.00 m/s

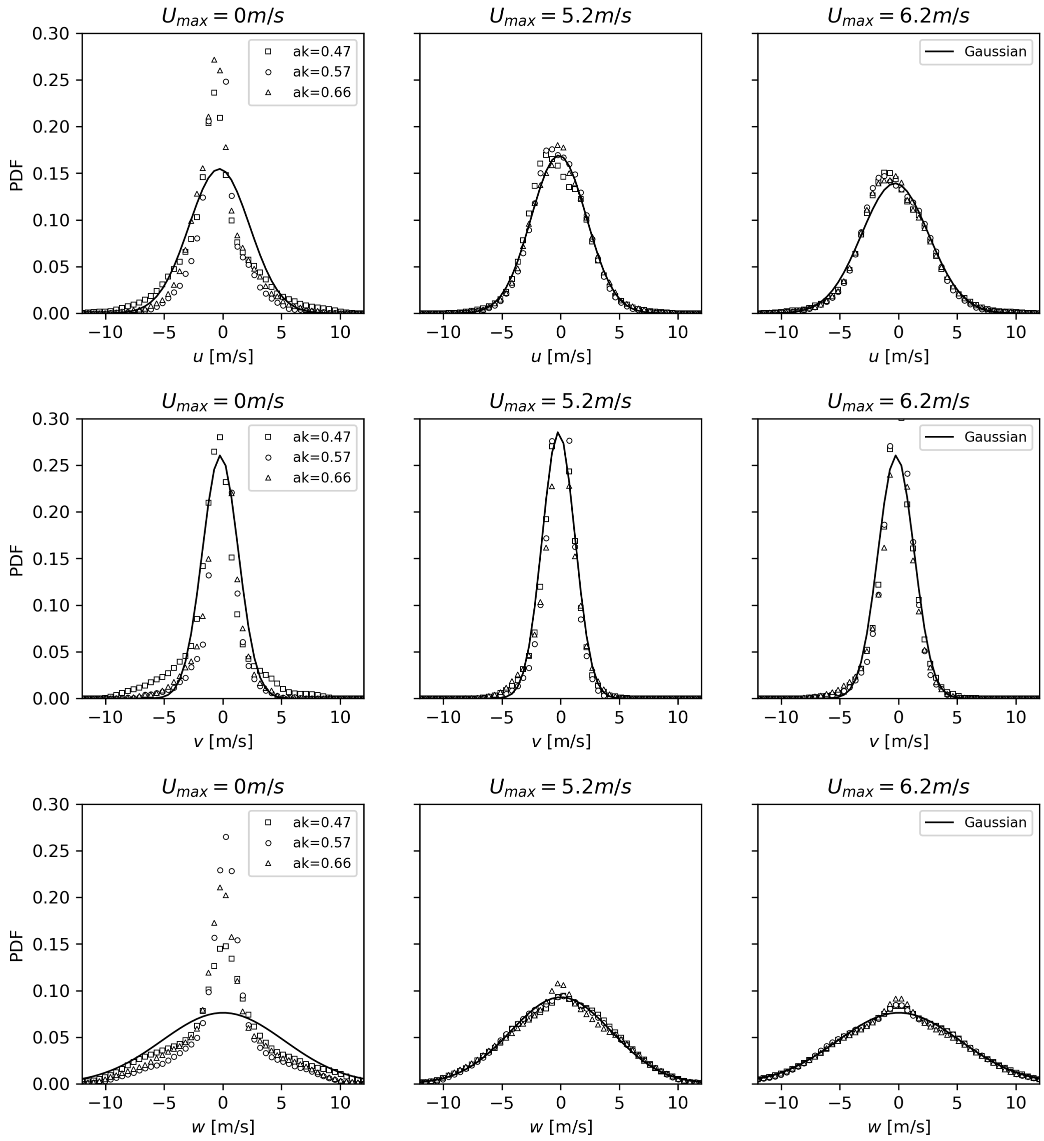

Figure 13. Probability distribution for the different velocity components for the different wind cases. Maximum values of Re are $Re_0 = 120$, $Re_{5.2} = 2700$ and $Re_{6.2} = 3200$; where the subscript refers to the correspondent U_{max}

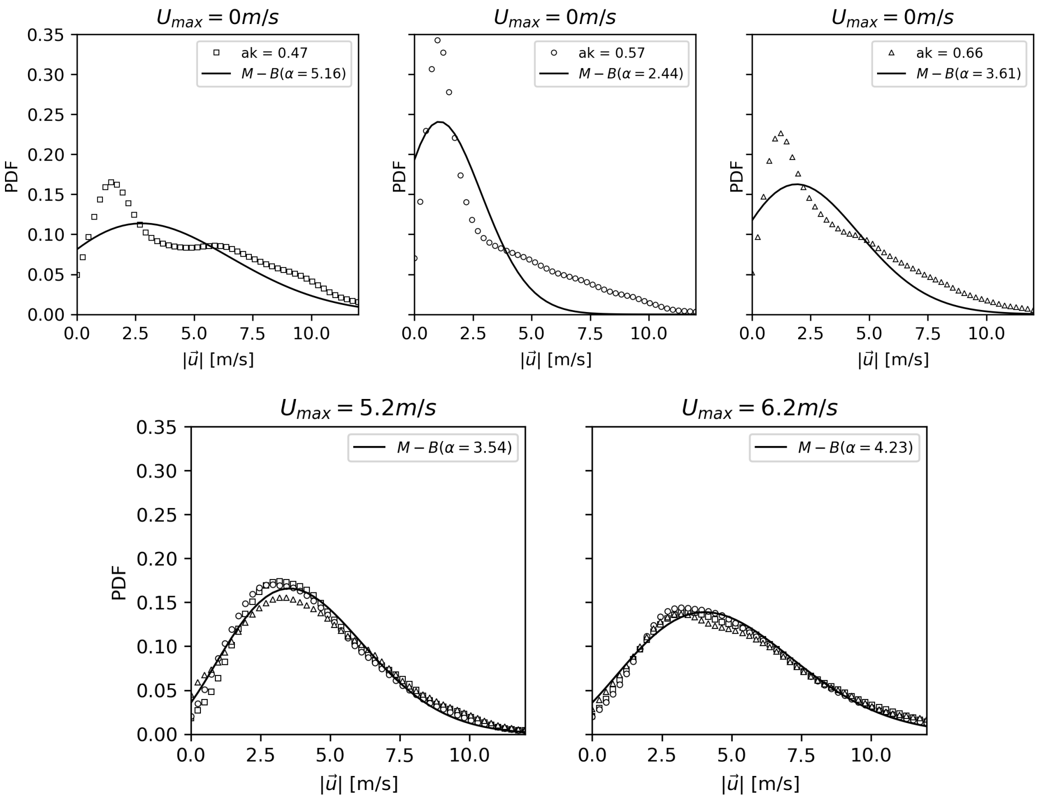

Figure 14. Probability distribution for the speed for the different wind cases.

In general, it is visible that the speed distributions for $U_{max} = 0$ are dependent on the values of ak and differs largely from the *M-B* distribution, while the other cases become independent of ak and follow closely the *M-B* distribution. When there is no wind, the data distributions present larger probability for extreme values, both towards zero and the maximum speed. This is just a confirmation that the velocity components do not present a Gaussian shape, which is a reasonable assumption as most droplet trajectories are parabolic where the velocity components would be statistically dependent. On the other hand, when wind is introduced, the speed distribution resembles closely the *M-B* distribution, therefore we can confirm the components of the velocity have Gaussian behaviour. Physically, this is a significant finding, because the Gaussian and *M-B* distributions of the velocity can be indicators of random processes, or in some cases of turbulent processes (Batchelor, 1953; Mouri et al., 2002; Vincent & Meneguzzi, 1991).

Aditionally, we could consider the effect that the wind conditions have on the drag forces of the droplets. Independently of the wind conditions, droplets moving through air will be affected by different factors, specifically the drag force is dependent on the velocity, the size of the droplet and their deformation through the air. Small droplets $D_e < 1\,\mathrm{mm}$ will have considerable drag because of the small Re, they follow the drag-Reynolds relation for rigid spheres ($C_D = \frac{24}{Re}[1+0.1935Re^{0.6305}]$). For larger droplets ($> 1\,\mathrm{mm}$), the deformation of the droplet is also important, in general, it has been found that the drag coefficient is larger for an oblate spheroid than for a sphere. On top of the drag coefficient variations due to the drop and its own dynamics, the effect of an external flow, like wind, should be consider also. The drag-Reynolds relation becomes fairly complicated because of all the parameters and their variations. Therefore we cannot assume that large droplets will be less affected by drag than small droplets. For example,

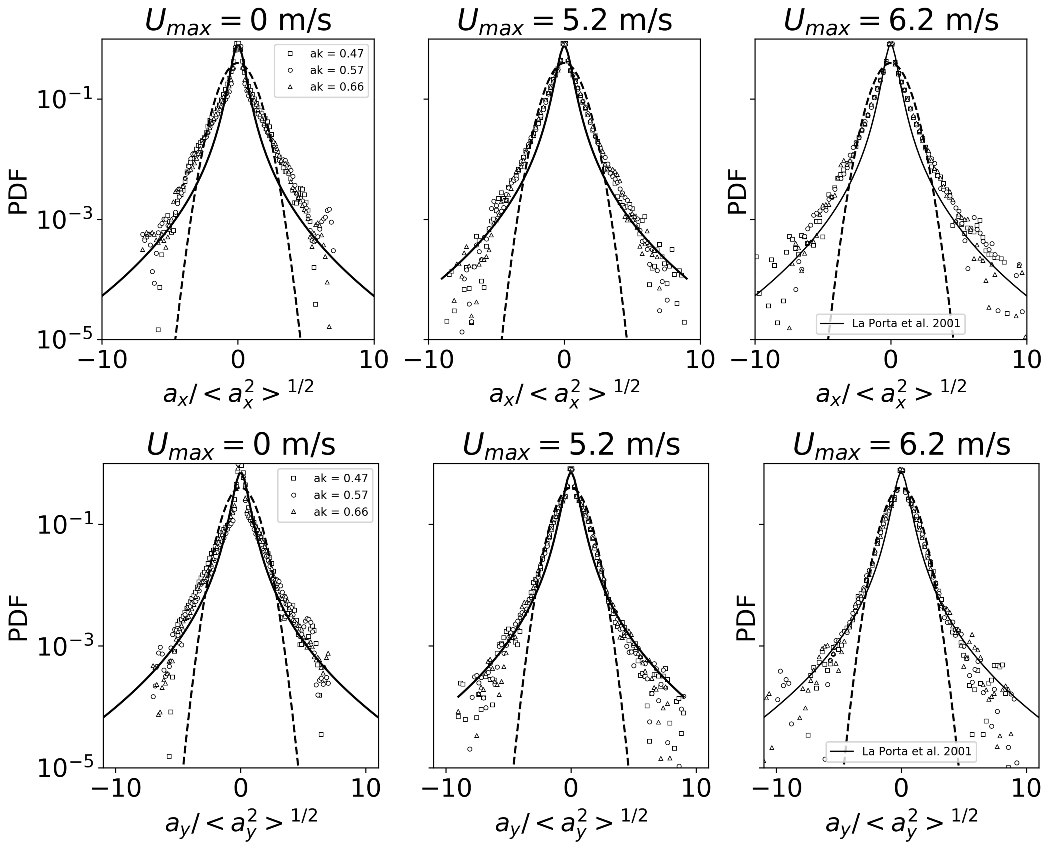

Figure 15. Probability distribution for the acceleration components for the different wind cases. Maximum values of Re_λ are $Re_{\lambda,0} = 42$, $Re_{\lambda,5.2} = 201$ and $Re_{\lambda,6.2} = 218$; where the subscript refers to the correspondent U_{max}

experimental data of water droplets falling in turbulent flows (Laws, 1941) has shown that for large drops the average drag coefficient is higher than in non turbulent flows. In addition, when studying large particles as flow tracers in Lagrangian methods (Xu & Bodenschatz, 2008), it was found that the acceleration PDF's where quite similar to those of the tracer particles, with the tails being weakly suppressed. This will suppose that the large particles also follow the turbulent flow at a certain degree. Analysis of the acceleration distributions can also be done to compare to this result.

3.2 Acceleration Distributions

Figure 15 shows the probability distribution of the acceleration components normalized by their standard deviation $a_i/ < a_i^2 >^{1/2}$ in the wind direction a_x and in the vertical direction a_y. The different ak are shown with different markers and each vertical panel shows a different cases of U_{max}. The dashed line represents the Gaussian distribution with the same standard deviation and the solid line shows the exponential distribution proposed by La Porta et al. (2001) and defined by:

$$C \exp\left(-\frac{a^2}{(1 + |a\beta/\sigma|^\gamma)\sigma^2}\right) \tag{10}$$

with $\beta = 0.539$, $\sigma = 0.508$, $\gamma = 1.588$, for the results presented here the constant $C = 0.67$. In all cases the probability for extreme cases is larger than the expected in a Gaussian distribution, but only for $U_{max} = 6.2\,\mathrm{ms^{-1}}$ the data resembles closely the distribution suggested by La Porta et al. (2001) where the extreme cases have the largest probability. In the graphs, it is visible that the tail values for the experimental data are not as high as those proposed by the distribution. This effect could be related to the level of turbulence in the flow and/or the size of the droplets. The level of turbulence is related to the values of Re_λ, which were calculated to be $Re_\lambda \leq 220$ for all the experiments. This values are in the lower limit of those studied by La Porta et al. (2001), where $Re_\lambda \geq 200$. On the other hand, the size of the droplets suggests that the droplets do not follow the flow, as passive tracers do, and therefore we do not expect them to behave in the same way. As mentioned before, Xu and Bodenschatz (2008) have also seen a similar effect on particles of large size compared to tracers, where the tail of the acceleration distributions is weakly suppressed when using large particles. Overall, we can confirm that the dynamics of the droplets produced after the wave splash is affected by the presence of wind even from velocities as low as $5\,\mathrm{ms^{-1}}$. The Lagrangian approach to the dynamics of particles shows a particular value in the measurement of accelerations. The Lagrangian approach also allows the study of several particles statistics and the statistics of turbulent flows, which is vital for the understanding of dispersion, the study of inertial particles and the development of the statistical models and simulations.

4 Conclusions

The initial distribution of droplets after a wave breaking event has been studied for droplets between $0.5\,\mathrm{mm} \leq D_e \leq 11\,\mathrm{mm}$. The influence of wind on this initial distributions has been addressed by comparing cases without wind and low wind velocities. The analysis shows that the distribution of droplets in all cases is in agreement with the Probability Distribution Function presented in previous studies for ligament-mediated spray formation. A shift of the mean diameter is found and correlated to the energy content of the breaking wave which could point out to a relation between the wave energy and the volume of the mean ligament created during breaking.

As for the velocities and accelerations, the distributions show noticeable differences between the cases without wind and the cases with wind. The presence of wind creates a turbulent flow that affect the movement of the droplets from its separation of the liquid bulk. When there is wind, the velocity components are normal distributed and the speed follows the *M-B* distribution as predicted by the theory of statistics in turbulent flows. On the other hand, the velocity components differs from the Gaussian shape when there is no wind, specially the speed has a very distinct shape from the *M-B* distribution and larger probability for extreme values. The findings are similar for the acceleration components where the distribution for the largest wind velocity has a more extended exponential tail, similar to experimental and numerical studies developed for Lagrangian trajectories in turbulent flows (Choi et al., 2004; Gerashchenko et al., 2008; Voth et al., 2001; Toschi & Bodenschatz, 2009).

Over all we have shown that the initial size distribution of droplets, or source function, for a wave impacting on the free surface, can be described by the proposed Γ-distribution. The mean and variance of this distribution is subjected to the properties of the breaker such as breaking type and energy content. The different mechanisms of droplet generation that can be present during the splashing of a breaking wave, need to be further studied individually and collectively, as in the nature these mechanisms are always combined and rarely isolated from each other. The influence of the flow surrounding the droplets is not negligible for the wind cases as it is obvious from the statistics. Furthermore, it can potentially be an important parameter in the droplet phenomenology, such as their vertical reach, their coalescence rates or even their residence times in the atmospheric boundary layers. Further studies should be directed to the understanding of these interactions.

The role of the large droplets is yet to be understood. The presented results shows that the generation of large droplets ($D_e > 1\,\mathrm{mm}$) during wave splashing is larger than proposed in previous studies. This could be consider in agreement with recent research that shows the production rates of these large droplets was higher than previously expected (Ortiz-Suslow et al., 2016). It is the largest droplets that can more easily breakup and generate more droplets when considering time evolution or increasing wind conditions. Therefore, their presence in the early stages of wave breaking and spray formation needs to be further studied. Furthermore, there is evidence of the influence of the flow in the large droplets in this study. Together with recent field studies (Lenain & Melville, 2017), this could suggest that large droplets have a longer lifetime in the atmospheric boundary layer than previously expected. Therefore, the processes from where these larger droplets are created and transported need to be better understood.

Acknowledgments

Funding from the Norwegian Research Council through the project 'Rigspray' (grant number 256435) is gratefully acknowledged. The authors will also like to acknowledge Alex Liberzon and the OpenPTV Software Consortium for the help with the use of OpenPTV. The help of Olav Gundersen in the experimental setup is gratefully acknowledge.

References

Andreas, E. L., Jones, K. F., & Fairall, C. W. (2010). Production velocity of sea spray droplets. *Journal of Geophysical Research: Oceans*, *115*(C12).

Batchelor, G. K. (1953). *The theory of homogeneous turbulence.* Cambridge university press.

Bodaghkhani, A., Dehghani, S.-R., Muzychka, Y. S., & Colbourne, B. (2016). Understanding spray cloud formation by wave impact on marine objects. *Cold Regions Science and Technology*, *129*, 114–136.

Brown, M. G., & Jensen, A. (2001). Experiments on focusing unidirectional water waves. *Journal of Geophysical Research: Oceans*, *106*(C8), 16917–16928.

Choi, J.-I., Yeo, K., & Lee, C. (2004). Lagrangian statistics in turbulent channel flow. *Physics of fluids*, *16*(3), 779–793.

Clift, R., Grace, J. R., & Weber, M. E. (2005). *Bubbles, drops, and particles.* Courier Corporation.

Consortium, O., et al. (2012). Openptv: Open source particle tracking velocimetry. *2012.,().*

Crowe, C. T., Schwarzkopf, J. D., Sommerfeld, M., & Tsuji, Y. (2011). *Multiphase flows with droplets and particles.* CRC press.

Dalziel, S. (2017). *Digiflow user guide, dalziel research partners.*

Dehghani, S., Naterer, G., & Muzychka, Y. (2016). Droplet size and velocity distributions of wave-impact sea spray over a marine vessel. *Cold Regions Science and Technology*, *132*, 60–67.

Fairall, C., Banner, M., Peirson, W., Asher, W., & Morison, R. (2009). Investigation of the physical scaling of sea spray spume droplet production. *Journal of Geophysical Research: Oceans*, *114*(C10).

Gerashchenko, S., Sharp, N., Neuscamman, S., & Warhaft, Z. (2008). Lagrangian measurements of inertial particle accelerations in a turbulent boundary layer. *Journal of fluid mechanics*, *617*, 255.

Kim, J.-T., & Chamorro, L. P. (2019). Lagrangian description of the unsteady flow induced by a single pulse of a jellyfish. *Physical Review Fluids*, *4*(6), 064605.

La Porta, A., Voth, G. A., Crawford, A. M., Alexander, J., & Bodenschatz, E. (2001). Fluid particle accelerations in fully developed turbulence. *Nature*, *409*(6823), 1017–1019.

Laws, J. O. (1941). Measurements of the fall-velocity of water-drops and raindrops. *Eos, Transactions American Geophysical Union*, *22*(3), 709–721.

Lenain, L., & Melville, W. K. (2017). Evidence of sea-state dependence of aerosol concentration in the marine atmospheric boundary layer. *Journal of Physical Oceanography*, *47*(1), 69–84.

Mordant, N., Crawford, A. M., & Bodenschatz, E. (2004). Experimental lagrangian acceleration probability density function measurement. *Physica D: Nonlinear Phenomena*, *193*(1-4), 245–251.

Mouri, H., Takaoka, M., Hori, A., & Kawashima, Y. (2002). Probability density function of turbulent velocity fluctuations. *Physical Review E*, *65*(5), 056304.

Mueller, J. A., & Veron, F. (2009). A sea state–dependent spume generation function. *Journal of physical oceanography*, *39*(9), 2363–2372.

Ortiz-Suslow, D. G., Haus, B. K., Mehta, S., & Laxague, N. J. (2016). Sea spray generation in very high winds. *Journal of the Atmospheric Sciences*, *73*(10), 3975–3995.

Ouellette, N. T., Xu, H., & Bodenschatz, E. (2006). A quantitative study of three-dimensional lagrangian particle tracking algorithms. *Experiments in Fluids*, *40*(2), 301–313. Retrieved from `https://doi.org/10.1007/s00348-005-0068-7` doi: 10.1007/s00348-005-0068-7

Pope, S. (1994). Lagrangian pdf methods for turbulent flows. *Annual review of fluid mechanics*, *26*(1), 23–63.

Rashid, T., Khawaja, H. A., & Edvardsen, K. (2016). Review of marine icing and anti-/de-icing systems. *Journal of Marine Engineering & Technology*, *15*(2), 79-87. Retrieved from `https://doi.org/10.1080/20464177.2016.1216734` doi: 10.1080/20464177.2016.1216734

Ryerson, C. C. (1990). Atmospheric icing rates with elevation on northern new england mountains, usa. *Arctic and Alpine Research*, *22*(1), 90–97.

Shnapp, R., Shapira, E., Peri, D., Bohbot-Raviv, Y., Fattal, E., & Liberzon, A. (2019). Extended 3d-ptv for direct measurements of lagrangian statistics of canopy turbulence in a wind tunnel. *Scientific reports*, *9*(1), 1–13.

Stokes, M., Deane, G., Prather, K., Bertram, T., Ruppel, M., Ryder, O., … Zhao, D. (2013). A marine aerosol reference tank system as a breaking wave analogue for the production of foam and sea-spray aerosols. *Atmospheric Measurement Techniques*, *6*(4), 1085.

Toschi, F., & Bodenschatz, E. (2009). Lagrangian properties of particles in turbulence. *Annual review of fluid mechanics*, *41*, 375–404.

Veron, F. (2015). Ocean spray. *Annual Review of Fluid Mechanics*, *47*, 507–538.

Veron, F., Hopkins, C., Harrison, E., & Mueller, J. (2012). Sea spray spume droplet production in high wind speeds. *Geophysical Research Letters*, *39*(16).

Villermaux, E., Marmottant, P., & Duplat, J. (2004). Ligament-mediated spray formation. *Physical review letters*, *92*(7), 074501.

Vincent, A., & Meneguzzi, M. (1991). The spatial structure and statistical properties of homogeneous turbulence. *Journal of Fluid Mechanics*, *225*, 1–20.

Voth, G. A., La Porta, A., Crawford, A. M., Bodenschatz, E., & Alexander, J. (2001). Measurement of particle accelerations in fully developed turbulence. *arXiv preprint physics/0110027*.

Xu, H., & Bodenschatz, E. (2008). Motion of inertial particles with size larger than kolmogorov scale in turbulent flows. *Physica D: Nonlinear Phenomena*, *237*(14-17), 2095–2100.